ROYAL SOCIETY
OF CHEMISTRY

COMMUNICATION

Tuning the electronic properties of monolayer and bilayer PtSe$_2$ *via* strain engineering†

Pengfei Li,[a] Lei Li[b] and Xiao Cheng Zeng*[ab]

The recently synthesized monolayer PtSe$_2$ belongs to the class of two-dimensional transition metal dichalcogenide (TMDC) materials (*Nano Lett.*, 2015, 15, 4013). Based on first-principles calculations, we show that the band gaps of monolayer and bilayer PtSe$_2$ can be tuned over a wide range *via* strain engineering. Both isotropic and uniaxial strains are investigated. For bilayer PtSe$_2$, the vertical out-of-plane strain is also considered. In most cases, the strain can reduce the band gap except for the bilayer PtSe$_2$ under the isotropic strain ($\varepsilon \leq 4\%$) for which the band gap can be slightly enlarged. Importantly, the monolayer can be transformed from the indirect-gap to the direct-gap semiconductor at the compressive strain of $\varepsilon_y = -8\%$. Moreover, the bilayer can undergo the semiconductor-to-metal (S–M) transition at a critical vertical strain due to the chemical interaction (p orbital coupling) between the Se atoms of the two opposite layers. Overall, the ability to modulate the band gap of monolayer and bilayer PtSe$_2$ over an appreciable range of strains opens up new opportunities for their applications in nano-electronic devices.

Introduction

Two dimensional (2D) graphene has attracted intensive research interest over the past ten years[1–5] due to its novel properties such as unconventional quantum Hall effect, superior electronic conductivity, and high mechanical strength. However, the zero-band gap apparently hinders the wide application of graphene in optoelectronic nanodevices. This situation has led to extensive efforts devoted to the exploration of other 2D materials with finite band gaps such as phosphorene,[6–10] BN,[11] transition-metal dichalcogenides (TMDCs),[12–17] and transition-metal

trichalcogenides (TMTCs).[18,19] The general formula of 2D TMDCs is MX$_2$, where M is a transition metal in groups 4–10 while X is a chalcogen. Depending on the combination of metal and chalcogen, bulk TMDCs display diverse properties, ranging from insulators (HfS$_2$), semiconductors (MoS$_2$, WS$_2$), semi-metals (WTe$_2$, TiSe$_2$), metals (NbS$_2$, VSe$_2$) to superconductors (NbSe$_2$, TaS$_2$).[20] Low-dimensional counterparts of bulk MX$_2$ may preserve certain bulk properties but can also bring new characteristics due to quantum confinement effects.[21–23] For example, low-dimensional TMDCs can offer new opportunities for research in many fields, such as in catalysis, energy storage, sensing and electronic devices.

To date, most experimental studies of 2D TMDCs have been mainly focused on semiconducting MX$_2$ with group 6 transition metals (Mo, W), *e.g.*, MoS$_2$, MoSe$_2$, and WSe$_2$. Recently, many other monolayer TMDCs beyond MoX$_2$ and WX$_2$ have been shown to exhibit unique physical or chemical properties as well. Specifically, Wang *et al.* reported a newly synthesized PtSe$_2$ monolayer.[24] Unlike the conventional method for the fabrication of MX$_2$ through exfoliation or chemical vapor deposition, the synthesis of PtSe$_2$ can be achieved *via* the direct deposition of Se atoms on a Pt substrate. Through angle-resolved photo-emission spectroscopy (ARPES) and band structure calculations, it is found that monolayer PtSe$_2$ is a semiconductor, contrary to the semimetal properties of its bulk counterpart. Moreover, the photo-degradation experiment suggests that monolayer PtSe$_2$ can serve as a visible light-driven photocatalyst.

Many previous theoretical studies[25–28] have shown that the electronic structures of 2D TMDCs can be notably modified by external electric fields or by in-plane strains. In this study, we show the strain-dependent electronic properties of mono-layer and bilayer PtSe$_2$ on the basis of the first-principles computations. Both isotropic and uniaxial in-plane strains are considered. In addition, for the bilayer PtSe$_2$, we also considered normal compressive strain (out-of-plane vertical strain). We found that monolayer PtSe$_2$ can maintain its indirect semiconducting character under strain except for the uniaxial compressive strain beyond -8% along the y direction (see below for definition),

^{a} *Hefei National Laboratory for Physical Sciences at Microscale and Department of Chemical Physics, University of Science and Technology of China, Hefei, Anhui 230026, China*

^{b} *Department of Chemistry, University of Nebraska-Lincoln, Lincoln, Nebraska 68588, USA. E-mail: xzeng1@unl.edu*

† Electronic supplementary information (ESI) available. See DOI: 10.1039/c6tc00130k

3106 | *J. Mater. Chem. C*, 2016, 4, 3106–3112

This journal is © The Royal Society of Chemistry 2016

which induce a transition from the indirect semiconductor to the direct one. In general, the strains can reduce the band gap of monolayer $PtSe_2$ regardless of the magnitude and direction of the strain. Under an isotropic in-plane strain, the tensile strain appears to be more effective for reducing the band gap of monolayer $PtSe_2$ than the compressive strain except for the case of 8% tensile strain. On the other hand, the trend is opposite in the case of uniaxial strain. For the bilayer $PtSe_2$, the isotropic in-plane compressive strain can enlarge the band gap first and then reduce the band gap, while the isotropic tensile strain reduces the band gap continuously. Hence, the strain-engineering behavior of monolayer or bilayer $PtSe_2$ is very different from that of MoS_2.[25] Furthermore, the reversible semiconductor-to-metal transition is predicted for the $PtSe_2$ bilayer under normal compressive strain in the critical range of $0.4 < \varepsilon \leq 0.45$. The transition stems from the p orbital coupling of the inner Se atoms of the two layers.

Computational methods

All the calculations are performed using the density functional theory within the generalized gradient approximation, as implemented in the Vienna *Ab initio* Simulation Package (VASP) 5.3.3 code.[29] The all-electron plane-wave basis set within the projector augmented wave (PAW) method is adopted with $5d^9 6s^1$ and $4s^2 4p^4$ treated as valence electrons for Pt and Se, respectively, and the Perdew–Burke–Ernzerhof (PBE) exchange–correlation functional is selected. The cutoff energy for expansion of the wavefunction into plane waves is set to be 360 eV, and a *k*-point set of $25 \times 25 \times 1$ is used for total-energy computation and a dense *k*-point set of $40 \times 40 \times 1$ is used for electronic structure computation. The conjugate-gradient scheme is employed for the geometric relaxation until the force on each atom is less than 0.01 eV $Å^{-1}$, and the total energy change is less than 1×10^{-5} eV. Sufficient vacuum space (≥ 15 Å) is used along the *z* direction (normal to the 2D sheet) to avoid spurious interaction among the periodic images. The van der Waals interaction originating from dynamical correlations between fluctuating charge distributions cannot be effectively described by the PBE functional. Hence, we incorporate the van der Waals interactions by adding a semi-empirical dispersion potential (*D*) to the conventional Kohn–Sham DFT energy, through a pair-wise force field following the Grimme's DFT-D3 method.[30]

Results and discussion

The bulk $PtSe_2$ belongs to the D_{3d}^3 ($P\bar{3}m1$) space group of the trigonal system.[31] As shown in Fig. 1(a), the monolayer $PtSe_2$ can be viewed as cleaved from the (0001) surface of the bulk $PtSe_2$, where one Pt atom layer is sandwiched between two Se layers. The optimized lattice parameter is 3.75 Å, very close to the experimental value of 3.70 Å.[24] The Pt–Se bond length and the total energy per atom of $PtSe_2$ *versus* isotropic in-plane strain are examined. As shown in Fig. 1(b), the Pt–Se bond length increases almost linearly with the increasing tensile strain, but shows a gentle decrease with the increasing compressive strain.
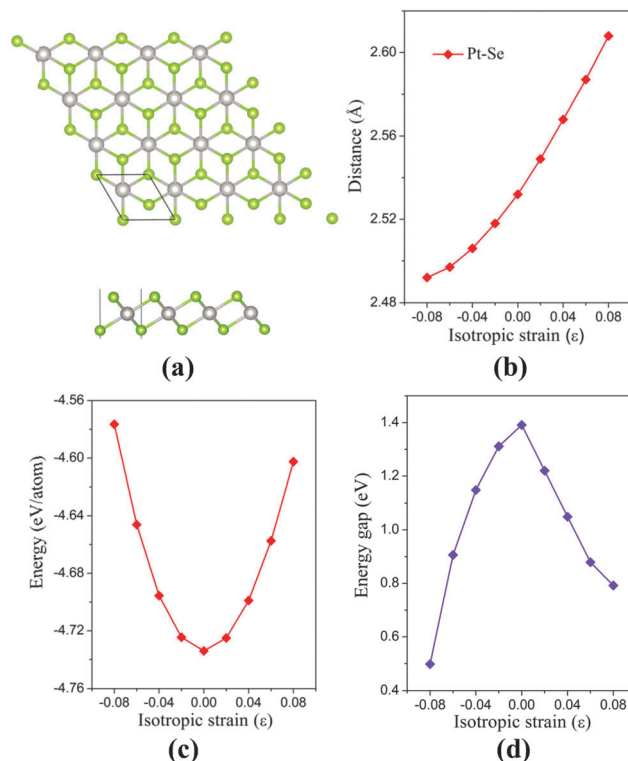

Fig. 1 (a) Top and side views of monolayer $PtSe_2$. The green and gray balls represent Pt and Se atoms, respectively. (b) Pt–Se bond length *versus* isotropic in-plane strain. (c) Total energy per atom of the monolayer $PtSe_2$ *versus* isotropic strain. (d) Computed band gap of monolayer $PtSe_2$ *versus* isotropic strain.

The bond length alteration surely correlates with the energy change. As shown in Fig. 1(c), the isotropic strain shows asymmetric quadratic dependence on the total energy per atom. The energy is −4.576 eV per atom at the compressive strain $\varepsilon = -8\%$, but is −4.602 eV per atom at the tensile strain of $\varepsilon = 8\%$. Therefore, from the energetic point of view, the tensile strain is easier to implement than the compressive strain.

The electronic structure of monolayer $PtSe_2$ under the isotropic strain is shown in Fig. 2(a) and (b). The strain-free monolayer $PtSe_2$ is an indirect semiconductor with a band gap of 1.39 eV, consistent with the previously predicted value of 1.41 eV (PBE).[32] The valence band maximum (VBM) and conduction band minimum (CBM) are located at ΓH and TL points (see Fig. 2(a) and (b)), respectively. Upon increasing the compressive strain, the VBM remains at the ΓH point, while the CBM is shifted downward (Fig. 2(a)). When the compressive strain reaches −4%, the UL point exhibits lower energy than the TL point, leading to the relocation of the CBM. In contrast, as shown in Fig. 2(b), the tensile strain can significantly lower the position of ΓH point so that the VBM is shifted from the ΓH to the VH point whose energy remains unchanged, regardless of the tensile strain. In addition, the CBM (TL point) is shifted downward with the increasing tensile strain. In general, the band gap of the monolayer $PtSe_2$ can be reduced by either the compressive or the tensile strain. As plotted in Fig. 1(d), the band gap of monolayer $PtSe_2$ decreases linearly from 1.39 to
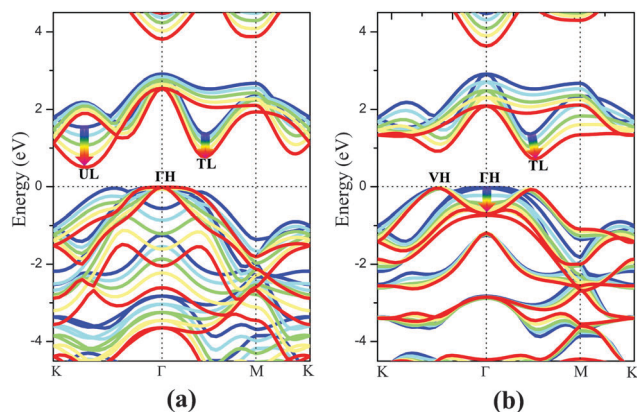
Fig. 2 Computed band structures of monolayer $PtSe_2$ under (a) isotropic compressive, and (b) isotropic tensile strain. The bands with different colors denote the band structures under different strain, i.e., blue ($\varepsilon = 0\%$), cyan ($\varepsilon = \pm 2\%$), green ($\varepsilon = \pm 4\%$), yellow ($\varepsilon = \pm 6\%$) and red ($\varepsilon = \pm 8\%$). The Fermi level is located at 0 eV.

several values of U and found for $U = 4$ eV, the relaxed lattice constant of the monolayer $PtSe_2$ is 3.725 Å, which is very close to the experimental value of 3.70 Å. The computed band structures of monolayer $PtSe_2$ under the isotropic strain $\varepsilon = -8\%$, 0% and 8% are plotted as shown in Fig. S1 (ESI†). It can be seen that the semiconducting character remains unchanged although the computed band gap is lowered by 0.1–0.4 eV for $U = 4$ eV.

To analyze the strain dependent electronic properties, the partial density of state (PDOS) and partial charge densities corresponding to the VBM and the CBM of the monolayer $PtSe_2$ at the isotropic strain of -8%, 0% and 8%, respectively, are plotted as shown in Fig. 3(a)–(f). As shown in Fig. 3(b) and (e), for the strain-free monolayer, the VBM (ΓH point) is mainly contributed by Se p orbitals and the coupling between the Pt d orbitals (mainly $d_{xy} + d_{x^2}$) and Se p orbitals. Yet the CBM (TL point) is mainly contributed by Pt $d_{yz} + d_{xz}$ orbitals and, to less extent, by Se p orbitals and Pt $d_{xy} + d_{x^2}$ orbitals. At the isotropic strain, as shown in Fig. 3(a), (c), (d) and (f), the VBM is mainly contributed by Se p orbitals and also slightly by Se-p and Pt-d coupling, different from the strain-free case. The isotropic strain significantly lowers the coupling between the Pt d orbitals and Se p orbitals near the VBM. However, the electronic component of the CBM under strain somewhat differs from that without strain. Fig. 2(a) and (b) clearly shows that, under isotropic strain, the change of band gap of monolayer $PtSe_2$ is mainly induced by the location change of CBM. As shown in Fig. 3(f), at a tensile strain of 8%, the CBM (TL point) is mainly contributed by the Pt $d_{xy} + d_{x^2}$ orbitals, Se p orbitals and somewhat by Pt $d_{yz} + d_{xz}$
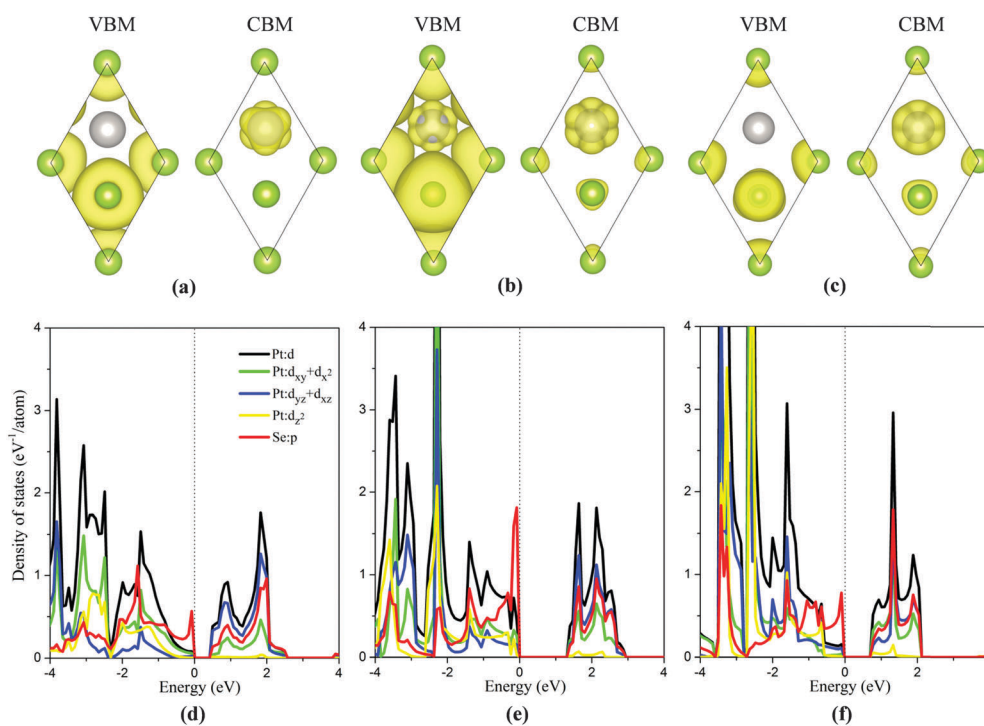
0.88 eV with the increasing tensile strain up to $\varepsilon = 6\%$, and then to 0.79 eV at $\varepsilon = 8\%$. However, the band gap of monolayer $PtSe_2$ is correlated parabolically with the compressive strain, decreasing from 1.39 to 0.5 eV at $\varepsilon = -8\%$. Moreover, it is known that semi-local DFT methods (such as the PBE functional) can markedly over-delocalize electrons. To address this issue, we performed an independent benchmark computation based on the DFT+U method as it can give more reasonable electronic properties than the semi-local DFT methods.[33,34] We examined

Fig. 3 Partial charge densities corresponding to the VBM and CBM, and partial densities of states (PDOS) of the monolayer $PtSe_2$ under isotropic strain of -8% (a and d), 0% (b and e) and 8% (c and f), respectively. Due to the specific symmetry, the contribution from d_{xy} is the same as that from d_{x^2}, and the contribution from d_{yz} is the same as that from d_{xz}. The isosurface value is 0.001.

3108 | J. Mater. Chem. C, 2016, **4**, 3106–3112

This journal is © The Royal Society of Chemistry 2016

orbitals, apparently different from the case of zero strain. We therefore conclude that the electronic component of CBM is changed by the tensile strain, causing the descent of CBM energy and band gap reduction for the monolayer PtSe$_2$. As for the monolayer PtSe$_2$ under compressive strain, Fig. 3(d) shows that the electronic component of CBM is little changed, and is still contributed mainly by the Pt d$_{yz}$ + d$_{xz}$ orbitals. But the repulsion of charge density of the d$_{yz}$ + d$_{xz}$ orbitals can be enhanced under compressive strain, thereby lowering the CBM (UL point) and resulting in band gap reduction for the monolayer PtSe$_2$.

We have also considered uniaxial strain along either the x or the y direction (see Fig. 4(a)). The computed electronic structure of the monolayer PtSe$_2$ based on the rectangle supercell under the uniaxial strain are shown in Fig. 4(e)–(i) and in the ESI,† Fig. S2. At zero strain, the VBM is located at the ΓH point and the CBM at the AL point (Fig. 4(g)). As in the case of the isotropic strain, the uniaxial strain along either the x- or the y-direction can significantly lower the energy of CBM, but makes little change to the VBM (less than 50 meV), thereby reducing the band gap of the PtSe$_2$ monolayer. Moreover, the

uniaxial compressive strain along either the x- or the y-direction does not change the VBM position (always at the Γ point), similar to the case of isotropic strain. Interestingly, the monolayer PtSe$_2$ undergoes the indirect-to-direct transition at the compressive strain of $\varepsilon_y = -8\%$ along the y direction, contrary to the isotropic strain. However, such a transition is not seen with the strain in the x direction even with a compressive strain of up to $\varepsilon_x = -8\%$. In Fig. 4(d), the change in the energy value of AL and ΓL points (with respect to the Fermi level) is plotted as a function of the strain ε_y. It can be seen that the energy difference ($E_{AL} - E_{\Gamma L}$) decreases almost linearly with the increasing compressive strain ε_y and becomes negative as ε_y is beyond -6%, causing an indirect-to-direct transition. Hence, we conclude that the indirect-to-direct transition can be attributed in part to the difference in strain dependence of E_{AL} and $E_{\Gamma L}$. The curves of band gap of monolayer PtSe$_2$ versus uniaxial strain are plotted as shown in Fig. 4(c). Notably, the uniaxial strain along x- and y-directions results in exactly the same modulation to the band gap in the strain range of -6% (0.96 eV gap) to 4% (1.19 eV gap) and to strain 8% (0.94 eV gap). A slight difference is seen at the uniaxial strain of -8% and 6%, where the band gap E_g ($\varepsilon_x = -8\%$) is 0.72 eV, E_g ($\varepsilon_y = -8\%$) is 0.65 eV, E_g ($\varepsilon_x = 6\%$) is 1.03 eV, and E_g ($\varepsilon_y = 6\%$) is 1.10 eV. Fig. 4(b) shows the plot of Pt–Se bond length versus uniaxial strain, where the slope of the two curves is quite different. As a result, the monolayer PtSe$_2$ shows direct semiconducting character at $\varepsilon_y = -8\%$ (Fig. 4(e)), but indirect semiconducting character at $\varepsilon_x = -8\%$ (Fig. 4(f)). In general, the uniaxial strain can modulate the band gap of the monolayer PtSe$_2$ but less strongly compared to the isotropic strain. The specific uniaxial strain ($\varepsilon_y = -8\%$), however, can transform the monolayer PtSe$_2$ from an indirect semiconductor to a direct one.

The 2D bilayer materials may possess different electronic properties from the monolayer counterpart due in part to the weak van der Waals interlayer interaction. First, the electronic structures of bilayer PtSe$_2$ under the isotropic strain are examined. Two different stacking patterns, namely, the AA-stacking and AB-stacking, are shown in Fig. 5(a). Our DFT computations show that both types of PtSe$_2$ bilayers are almost degenerate in energy and also exhibit similar band structures. As shown in Fig. 5(c) and (e), both PtSe$_2$ bilayers are indirect semiconductors with a band gap of 0.99 eV. The VBM and CBM are located at VH and TL points (see Fig. 5(c) and (e)), respectively. With the compressive strain, the position of VBM changes from the VH to the ΓH point but with small energy variation (< 50 meV), while the CBM is kept at the TL point and moves up slightly for $\varepsilon \leq 4\%$ and then downward to the Fermi level. As a result, the band gap of PtSe$_2$ bilayers firstly increases for $\varepsilon \leq 4\%$, from 0.99 to 1.09 eV (see Fig. 5(b)) and then decreases for $\varepsilon \geq 4\%$, from 1.09 to 0.43 or 0.51 eV (Fig. 5(b)). Fig. 5(d) and (f) shows the tensile strain-dependent band structures of both PtSe$_2$ bilayers, where one can see that the position of VBM moves slightly toward the K point with little energy change while the CBM is shifted toward the Fermi level. Therefore, the tensile strain reduces the band gap of PtSe$_2$ bilayers from 0.99 eV to 0.48 or 0.56 eV (Fig. 5(b)).
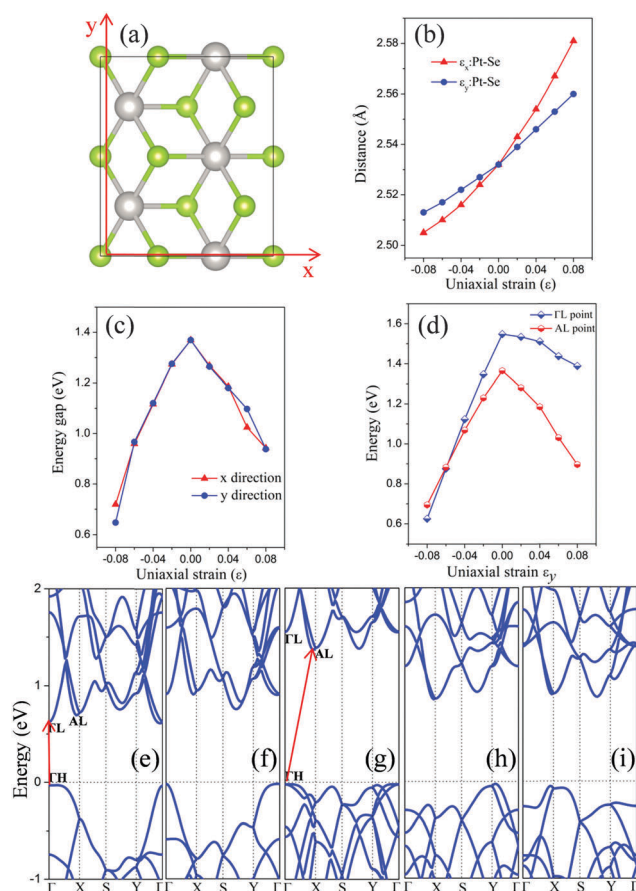

Fig. 4 (a) A rectangle supercell of monolayer PtSe$_2$ where x- and y-directions are defined. (b and c) Pt–Se bond length and band gap of monolayer PtSe$_2$ versus uniaxial strain, respectively. (d) The energy of the AL and ΓL points with respect to the Fermi level versus ε_y. Computed band structure of monolayer PtSe$_2$ with strain values of (e) $\varepsilon_y = -8\%$, (f) $\varepsilon_x = -8\%$, (g) $\varepsilon = 0\%$, (h) $\varepsilon_x = 8\%$ and (i) $\varepsilon_y = 8\%$. The Fermi level is set to be 0 eV.
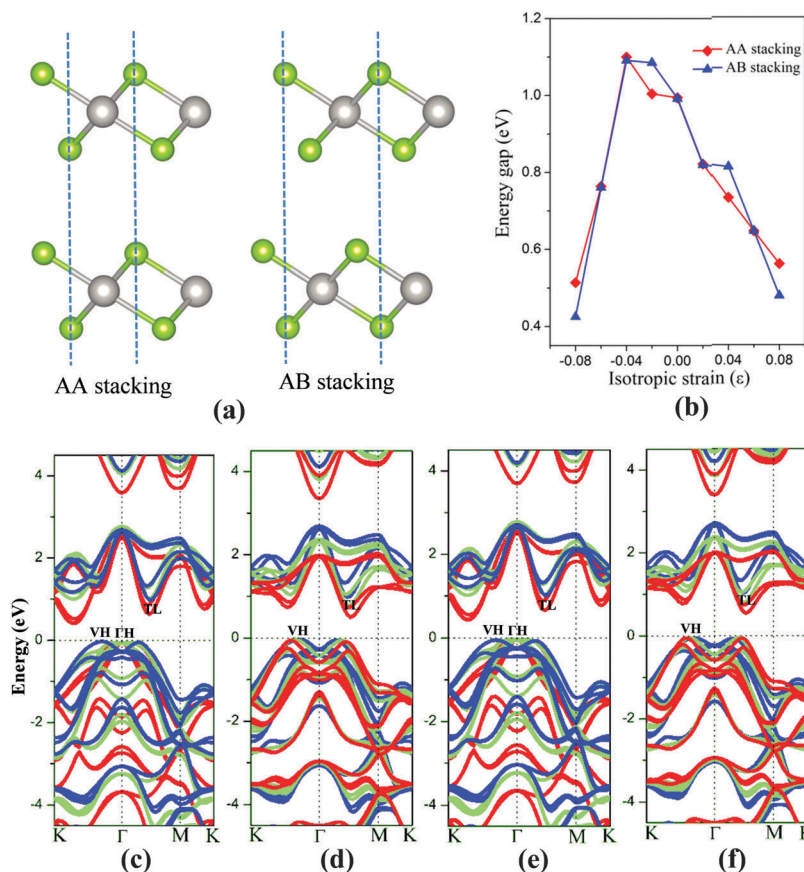
Fig. 5 (a) Atomic structure of two kinds of $PtSe_2$ bilayers. (b) Band gap of $PtSe_2$ bilayers *versus* isotropic strain. Computed band structure of AA stacking bilayers under (c) $\varepsilon = -8$ to 0%, (d) $\varepsilon = 0–8\%$ and AB stacking bilayers under (e) $\varepsilon = -8$ to 0%, (f) $\varepsilon = 0–8\%$. The bands with different colors represent the band structures under various strain values, *i.e.*, blue ($\varepsilon = 0\%$), green ($\varepsilon = \pm 4\%$) and red ($\varepsilon = \pm 8\%$). The Fermi level is located at 0 eV.
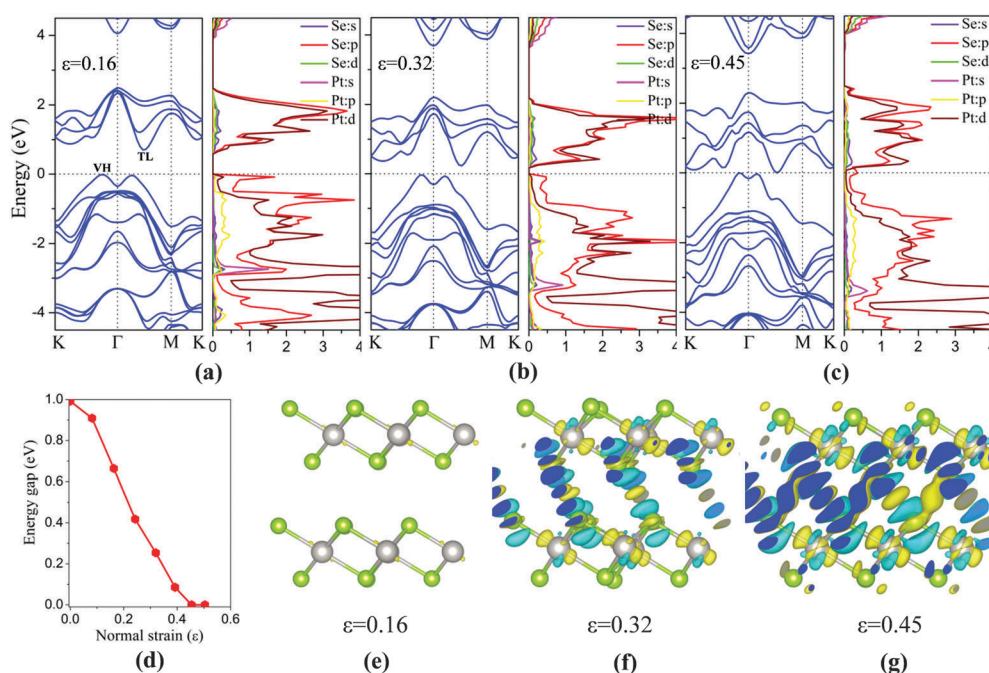

Fig. 6 (a–c) Computed band structure and partial densities of states of $PtSe_2$ bilayer under three different VCS values, with the corresponding differential charge densities plotted in (e–g). The Fermi level is located at 0 eV. (d) Band gap of bilayer *versus* normal strain.

3110 | *J. Mater. Chem. C*, 2016, **4**, 3106–3112

This journal is © The Royal Society of Chemistry 2016

Besides the in-plane strain, the electronic structures of the bilayer can also be modulated by applying an out-of-plane vertical strain. Taking the AB-stacking $PtSe_2$ bilayer as an example, the vertical compressive strain (VCS) is defined as $\varepsilon = (d_0 - d)/d_0$ where d_0 and d are the equilibrium and constrained interlayer distance, respectively. In the constrained configuration, the positions of the Pt atoms remain unchanged while other atoms are relaxed. The band structures of the bilayer under different VCS values are shown in Fig. 6(a)–(c), where it can be seen that the double degeneracy is lifted gradually due to the increasing interlayer chemical interaction as the interlayer distance decreases. The VBM is still located at the VH point with little change in energy, while the CBM (TL point) is shifted towards the Fermi level as the VCS increases, thereby reducing the band gap (Fig. 6(d)). It is interesting that the semiconductor-to-metal (S–M) transition occurs when the VBM and CBM crosses the Fermi level at the critical VCS ($0.4 < \varepsilon \leq 0.45$; see Fig. 6(c)). To assess the experimental feasibility of the S–M transition, we estimated the required pressure as done previously by others.[35,36] The applied pressure (P) is calculated from the energy cost per unit cell in reducing the interlayer distance by $\Delta d = d_0 - d$, that is, $P = (E_0 - E)/((d_0 - d) \times A)$, where A is the area of unit cell, and E and E_0 are the energies of strained and unstrained bilayers. As a result, the estimated transition pressure is between 1.2 and 3.6 GPa.

To gain more insights into the electronic properties of the bilayer under VCS, the PDOSs are computed (Fig. 6(a)–(c)). With the increasing VCS, the contribution to the CBM from Pt d and Se p orbitals increases, while that to the VBM from Se p orbitals decreases. From Fig. 6(c), it is seen that density of states near the Fermi level is mostly contributed by Se p orbitals, giving the metal character of the bilayer. This is due to the enhanced interlayer interaction that leads to the p orbital interaction of the inner Se atoms of the two opposite layers. This conclusion can be further supported through redistribution of the charges, computed by taking the difference between the total charge of the bilayer and the two isolated $PtSe_2$ layers (see Fig. 6(e)–(g)). The redistribution of the charge mainly arises around the inner Se atoms of the two layers. As expected, for a low VCS ($\varepsilon \leq 0.16$), almost no charge redistribution is observed. With the increasing VCS, the degree of charge redistribution also increases, indicating enhanced Se–Se interaction which can lead to the S–M transition.

Conclusion

In conclusion, we investigate band-gap engineering of semiconducting $PtSe_2$ monolayer and bilayer through applied isotropic, uniaxial, as well as vertical strains based on the first-principles calculations. Our electronic structure computations demonstrate that the electronic properties of $PtSe_2$ monolayer and bilayer are dependent on both the magnitude and direction of the strain. As a result, the band gap can be tuned over a wide range. In addition, the $PtSe_2$ monolayer can transform from an indirect semiconductor into a direct one when the compressive strain $\varepsilon_y = -8\%$, which may be exploited for special applications in nanoelectronics.

Furthermore, a reversible semiconductor-to-metal transition is predicted for the $PtSe_2$ bilayer under critical VCSs ($0.4 < \varepsilon \leq 0.45$, 1.2 GPa $< P \leq 3.6$ GPa). This stems from the p orbital coupling of the inner Se atoms of the two layers. The possibility of reversibly tuning the band gap by about 1.0 eV through application of different strains will render the 2D $PtSe_2$ a potential candidate for optoelectronic applications.

References

1 K. S. Novoselov, A. K. Geim, S. V. Morozov, D. Jiang, Y. Zhang, S. V. Dubonos, I. V. Grigorieva and A. A. Firsov, *Science*, 2014, **306**, 666.

2 K. S. Novoselov, A. K. Geim, S. V. Morozov, D. Jiang, M. I. Katsnelson, I. V. Grigorieva, S. V. Dubonos and A. A. Firsov, *Nature*, 2005, **438**, 197.

3 K. S. Novoselov, E. McCann, S. V. Morozov, V. I. Falko, M. I. Katsnelson, U. Zeitler, D. Jiang, F. Schedin and A. K. Geim, *Nat. Phys.*, 2006, **2**, 177.

4 Y. B. Zhang, Y. W. Tan, H. L. Stormer and P. Kim, *Nature*, 2005, **438**, 201.

5 Q. Tang, Z. Zhou and Z. Chen, *Nanoscale*, 2013, **5**, 4541.

6 L. Li, Y. Yu, G. J. Ye, Q. Ge, X. Ou, H. Wu, D. Feng, X. H. Chen and Y. Zhang, *Nat. Nanotechnol.*, 2014, **9**, 372.

7 J. Dai and X. C. Zeng, *J. Phys. Chem. Lett.*, 2014, **5**, 1289.

8 Y. H. Xu, J. Dai and X. C. Zeng, *J. Phys. Chem. Lett.*, 2015, **6**, 1996.

9 M. H. Wu, H. Fu, L. Zhou, K. L. Yao and X. C. Zeng, *Nano Lett.*, 2015, **15**, 3557.

10 H. Guo, N. Lu, J. Dai, X. J. Wu and X. C. Zeng, *J. Phys. Chem. C*, 2014, **118**, 14051.

11 D. Pacile, J. C. Meyer, C. O. Girit and A. Zettl, *Appl. Phys. Lett.*, 2008, **92**, 133107.

12 B. Radisavljevic, A. Radenovic, J. Brivio, V. Giacometti and A. Kis, *Nat. Nanotechnol.*, 2011, **6**, 147.

13 Q. H. Wang, K. Kalantar-Zadeh, A. Kis, J. N. Coleman and M. S. Strano, *Nat. Nanotechnol.*, 2012, **7**, 699.

14 H. S. S. Ramakrishna Matte, A. Gomathi, A. K. Manna, D. J. Late, R. Datta, S. K. Patiand and C. N. R. Rao, *Angew. Chem., Int. Ed.*, 2010, **49**, 4059.

15 J. Feng, L. Peng, C. Wu, X. Sun, S. Hu, C. Lin, J. Dai, J. Yang and Y. Xie, *Adv. Mater.*, 2012, **24**, 1969.

16 P. J. Jeon, S. Min, J. S. Kim, S. R. A. Raza, K. Choi, H. S. Lee, Y. T. Lee, D. K. Hwang, H. J. Choi and S. Im, *J. Mater. Chem. C*, 2015, **3**, 2751.

17 H. Fang, S. Chuang, T. C. Chang, K. Takei, T. Takahashi and A. Javey, *Nano Lett.*, 2012, **12**, 3788.

18 J. Dai and X. C. Zeng, *Angew. Chem., Int. Ed.*, 2015, **54**, 7572.

19 M. Li, J. Dai and X. C. Zeng, *Nanoscale*, 2015, **7**, 15385.

20 M. Chhowalla, H. S. Shin, G. Eda, L. Li, K. P. Loh and H. Zhang, *Nat. Chem.*, 2013, **5**, 263.

This journal is © The Royal Society of Chemistry 2016

J. Mater. Chem. C, 2016, **4**, 3106–3112 | **3111**

21 T. Cao, G. Wang, W. Han, H. Ye, C. Zhu, J. Shi, Q. Niu, P. Tan, E. Wang, B. Liu and J. Feng, *Nat. Commun.*, 2012, **3**, 887.

22 H. Zeng, J. Dai, W. Yao, D. Xiao and X. Cui, *Nat. Nanotechnol.*, 2012, **7**, 490.

23 K. F. Mak, K. He, J. Shan and T. F. Heinz, *Nat. Nanotechnol.*, 2012, **7**, 494.

24 Y. Wang, L. Li, W. Yao, S. Song, J. T. Sun, J. Pan, X. Ren, C. Li, E. Okunishi, Y. Q. Wang, E. Wang, Y. Shao, Y. Y. Zhang, H. Yang, E. F. Schwier, H. Iwasawa, K. Shimada, M. Taniguchi, Z. Cheng, S. Zhou, S. Du, S. J. Pennycook, S. T. Pantelides and H. J. Gao, *Nano Lett.*, 2015, **15**, 4013.

25 P. Lu, X. Wu, W. Guo and X. C. Zeng, *Phys. Chem. Chem. Phys.*, 2012, **14**, 13035.

26 N. Lu, H. Guo, L. Li, J. Dai, L. Wang, W. Mei, X. Wu and X. C. Zeng, *Nanoscale*, 2014, **6**, 2879.

27 A. Ramasubramaniam, D. Naveh and E. Towe, *Phys. Rev. B: Condens. Matter Mater. Phys.*, 2011, **84**, 205325.

28 P. Johari and V. B. Shenoy, *ACS Nano*, 2012, **6**, 5449.

29 G. Kresse and J. Furthmuller, *Phys. Rev. B: Condens. Matter Mater. Phys.*, 1996, **54**, 11169.

30 S. Grimme, J. Antony, S. Ehrlich and S. Krieg, *J. Chem. Phys.*, 2010, **132**, 154104.

31 G. Y. Guo and W. Y. Liang, *J. Phys. C: Solid State Phys.*, 1986, **19**, 995.

32 H. L. Zhuang and R. G. Hennig, *J. Phys. Chem. C*, 2013, **117**, 20440.

33 V. I. Anisimov, F. Aryasetiawan and A. I. Lichtenstein, *J. Phys.: Condens. Matter*, 1997, **9**, 767.

34 P. Guss, M. E. Foster, B. M. Wong, F. P. Doty, K. Shah, M. R. Squillante, U. Shirwadkar, R. Hawrami, J. Tower and D. Yuan, *J. Appl. Phys.*, 2014, **115**, 034908.

35 L. Kou, B. Yan, F. Hu, S. Wu, T. O. Wehling, C. Felser, C. Chen and T. Frauenheim, *Nano Lett.*, 2013, **13**, 6251.

36 L. Kou, S. Wu, C. Felser, T. Frauenheim, C. Chen and B. Yan, *ACS Nano*, 2014, **8**, 10448.